


Cite this: *RSC Adv.*, 2023, 13, 21510

NO_x degradation ability of S-g-C₃N₄/MgAl-CLDH nanocomposite and its potential application in cement-based materials

Zhengxian Yang,^a Xiaoli Xiong,^a Xueyuan Yan,^a Shengyang Luo,^a Yong Zhang,^{a*} Bruno Briseghella^a and Giuseppe Carlo Marano^b

In this study a new photocatalytic nanocomposite, S-g-C₃N₄/MgAl-CLDH, was synthesized and implemented into cement mortar by internal mixing or coating. The photocatalytic NO_x degradation efficiency of the S-g-C₃N₄/MgAl-CLDH and photocatalytic mortar was investigated. The NO_x degradation efficiency and photoluminescence spectra of S-g-C₃N₄/MgAl-CLDH after being immersed in the simulated concrete pore solution were evaluated to assess its chemical stability. The results show that compared with S-g-C₃N₄, the S-g-C₃N₄/MgAl-CLDH exhibits a narrower bandgap (2.45 eV), a lower photogenerated electron–hole pair recombination rate and a higher specific surface area (36.86 m² g^{−1}). After 21 min of visible light irradiation, the NO_x degradation rate of S-g-C₃N₄/MgAl-CLDH achieves 100% as compared to merely 81.5% of S-g-C₃N₄. After being submerged in simulated concrete pore solution, the S-g-C₃N₄/MgAl-CLDH exhibits only a slight decrease of 5% in degradation rate after 12 min of irradiation, confirming a good compatibility and stability in cement-based materials. The NO_x degradation ability of the internally mixed mortar is enhanced with an increase in the dosage of S-g-C₃N₄/MgAl-CLDH. For coated mortar, in contrast, a decline in NO_x degradation rate is observed after 5 layers of coating owing to the lower porosity of mortar after excessive coating.

Received 24th June 2023

Accepted 12th July 2023

DOI: 10.1039/d3ra04243j

rsc.li/rsc-advances

1. Introduction

Nitrogen oxides (NO_x) represent a notable category of atmospheric pollutants that give rise to substantial environmental issues, such as the emergence of photochemical smog, the occurrence of acid rain and the development of respiratory diseases in human beings.^{1,2} Adoption of efficacious approaches aiming at preventing or controlling NO_x pollution is urgently in need. One approach that has gained considerable attention is the implementation of photocatalytic techniques, in particular incorporating photocatalysts into various construction materials such as cement-based materials.^{3,4} Currently, TiO₂ is known as one of the most widely used photocatalysts. It has however drawbacks such as large band gap width (3.2 eV), high rate of recombination of photogenerated electron–hole pairs, low utilization of visible light and susceptibility to aggregation.⁵ Compared to TiO₂, a new semiconductor photocatalytic material, graphite carbon nitride (g-C₃N₄), has a smaller band gap width (2.7 eV), a wider range of response to visible light and a lower cost.⁶ It is reported that g-C₃N₄ can be stimulated by

ultraviolet-visible (UV-vis) light and has been utilized in various depollution fields such as degradation of organic pollutants and the mitigation of air pollution.⁶ Nevertheless, due to insufficient absorption of UV-vis light, the g-C₃N₄ exhibits a relatively low photocatalytic efficiency, greatly limiting its practical applications.⁷ In this respect, researchers have proposed various modification approaches for g-C₃N₄, including non-metal element doping⁷ and semiconductor composites.^{8,9} To begin with, the doping of non-metal elements into g-C₃N₄ can reduce the band gap width and broaden the range of light response, thereby enhancing its photocatalytic performance. Liu *et al.*¹⁰ reported that compared to pure g-C₃N₄, Cl-g-C₃N₄ exhibited approximately a five-fold increase in specific surface area, leading to enhanced photocatalytic performance. Specifically, the degradation efficiency of Rhodamine B (RhB) using Cl-g-C₃N₄ was approximately 12.9 times higher than that of g-C₃N₄. Wang *et al.*¹¹ synthesized sulfur (S) doped g-C₃N₄ (S-g-C₃N₄). Compared to g-C₃N₄, the S-g-C₃N₄ exhibited an absorption edge shift from 455 nm to 470 nm, indicating enhanced visible light absorption capability. Meanwhile the band gap width also reduced from 2.70 eV to 2.63 eV, indicating a decrease in the recombination rate of photogenerated electron–hole pairs. Notably, the photocatalytic efficiency of S-g-C₃N₄ in the degradation of methanol (CH₃OH) was nearly twice that of g-C₃N₄.

Another modification method is semiconductor composition, which involves combining two different semiconductor

^aJoint International Research Laboratory of Deterioration and Control of Coastal and Marine Infrastructures and Materials, College of Civil Engineering, Fuzhou University, Fuzhou 350108, China. E-mail: y.zhang@fzu.edu.cn

^bDepartment of Structural, Geotechnical and Building Engineering, Politecnico di Torino, Corso Duca degli Abruzzi, 24-10129 Torino, Italy



materials with distinct band structures. The energy level difference between the two semiconductors allows for the injection of photogenerated charge carriers from one semiconductor to the energy level of the other, facilitating efficient charge separation and promoting enhanced photocatalytic reaction efficiency.¹² Gu *et al.*¹³ prepared O-g-C₃N₄/TiO₂ heterostructured photocatalysts using an *in situ* solvothermal method. This composite combines the advantages of both components, such as the higher light utilization efficiency of O-g-C₃N₄ and the larger surface area of TiO₂, effectively enhancing the photocatalytic performance. The results indicate that the optimized O-g-C₃N₄/TiO₂ composite exhibits a photocatalytic performance 6.1 times higher than that of a physical mixture of TiO₂ and O-g-C₃N₄. Xiong *et al.*¹⁴ synthesized g-C₃N₄/CoAl-LDH using the hydrothermal method, and found that the incorporation of g-C₃N₄ into CoAl-LDH enhances the photocatalytic activity towards Cr(VI). The enhanced photocatalytic activity is mainly attributed to the synergistic effect of the heterojunction electric field at the interface between g-C₃N₄ and CoAl-LDH, which accelerates electron transfer and the separation of photogenerated electron-hole pairs. Zheng *et al.*¹⁵ prepared MgAl-LDO@g-C₃N₄ composite material using a hydrothermal and calcination method and found that MgAl-LDO@g-C₃N₄ exhibits superior photocatalytic RhB removal capability compared to Mg-Al-LDO. This can be attributed to the narrow bandgap structure for effective visible light response and the intimate interface for rapid charge transfer and migration.

Noteworthy, the incorporation of g-C₃N₄ in cement-based materials suffers from challenges owing to its chemical instability in highly alkaline environment.^{16,17} Great opportunities lie in the utilizations of layered double hydroxides (LDH), a group of compounds consisting of laminates made up of metal oxides and possessing high alkaline resistance. Of particular interest is that the LDH phases have a molecular structure that resembles cement hydration products.^{18,19} As a result, it demonstrates excellent compatibility with cement-based materials. As such, LDH can serve as ideal supportive substrates for photocatalysts.^{20,21} Huang *et al.*²² prepared a group of g-C₃N₄/CoAl-LDH nanocomposites with different g-C₃N₄ content and immersed them into simulated concrete pore solution. They found only a slight increase in photoluminescence (PL) intensity for g-C₃N₄/CoAl-LDH after alkaline treatment. In contrast, a significant increase was observed in the case of g-C₃N₄. This suggests that the alkaline environment has a lesser impact on the g-C₃N₄/CoAl-LDH nanocomposite as opposed to g-C₃N₄. Furthermore, the degradation efficiency of NO_x improves in the g-C₃N₄/CoAl-LDH nanocomposites as the g-C₃N₄ content increases. This improvement can primarily be attributed to the effective combination of g-C₃N₄ with LDH, which facilitates the separation and transfer of photo-induced charge carriers.

The application of g-C₃N₄ for the degradation of NO_x exhibits considerable promise from both environmental and economic perspectives, particularly when implemented in cement-based materials. In order to improve the disadvantages of g-C₃N₄ including low visible light utilization, high photogenerated electron-hole pairs recombination rate and poor alkaline resistance, this study employed sulfur for the modification of g-

C₃N₄ through doping. Then, S-g-C₃N₄/MgAl-CLDH nanocomposite was synthesized using electrostatic self-assembly method. A range of analytical techniques was utilized to characterize the physicochemical properties of S-g-C₃N₄/MgAl-CLDH, including X-ray diffraction (XRD), X-ray photoelectron spectroscopy (XPS), Fourier transform infrared spectra (FTIR), UV-vis diffuse reflectance spectroscopy (UV-vis DRS), Brunauer-Emmett-Teller (BET), transmission electron microscopy (TEM) and scanning electron microscopy coupled with energy dispersive X-ray (SEM-EDX). Furthermore, the photocatalytic performance of S-g-C₃N₄/MgAl-CLDH was analyzed through RhB and NO_x degradation tests. Lastly, to assess the application potential of S-g-C₃N₄/MgAl-CLDH in cement-based materials, the stability of its NO_x degradation ability in simulated concrete pore solution was examined. The NO_x degradation ability of cement mortar loaded with S-g-C₃N₄/MgAl-CLDH, by internal mixing or coating, was investigated.

2. Experimental

2.1. Raw materials

All chemical reagents were supported from National Medicine Group Chemical Reagent Co., Ltd., China. The main information of each reagent is shown in Table 1. The ordinary Portland cement (OPC), P.O 42.5, compliant with the Chinese standard GB175-2007, was utilized in the study. The chemical compositions of the OPC were determined using X-ray fluorescence (XRF) analysis and are presented in Table 2. Deionized water and standard sand, as per Chinese standard GB/T 14684-2022, were employed for preparation of cement mortar.

2.2. Synthesis of S-g-C₃N₄/MgAl-CLDH composites

For the preparation of g-C₃N₄, 2 g of melamine precursor was placed in a muffle furnace, heated up to 550 °C with a heating rate of 3 °C min⁻¹, and held for calcination for 2 h. After cooling to room temperature, the light yellow colored g-C₃N₄ was obtained, which was then ground into powder. The synthesis of

Table 1 Information of chemical reagents

	Chemical formula	Purity	Molecular mass
Ethanol anhydrous	C ₂ H ₆ O	AR	46.07
Thiourea	CH ₄ N ₂ S	AR	76.12
Calcium hydroxide	Ca(OH) ₂	AR	74.09
Hydrochloric acid	HCl	AR	34.46
Potassium nitrate	KNO ₃	AR	101.10
Rhodamine B	C ₂₈ H ₃₁ ClN ₃ O ₃	AR	479.01
Hydrotalcite	Mg ₆ Al ₂ (OH) ₁₆ CO ₃ ·4H ₂ O	AR	603.98
Melamine	C ₃ H ₆ N ₆	AR	126.12

Table 2 Main chemical composition of OPC (wt%)

CaO	SiO ₂	Al ₂ O ₃	Fe ₂ O ₃	SO ₃	Other
64.21	20.83	6.22	2.87	1.82	4.05



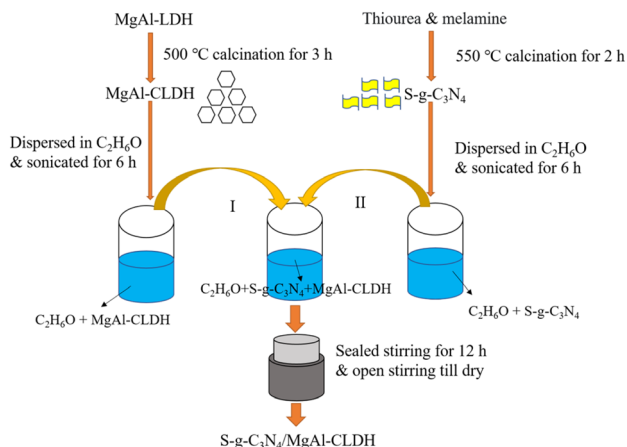


Fig. 1 Schematic diagram of the synthesis process of S-g-C₃N₄/MgAl-CLDH photocatalytic composite.

the S-g-C₃N₄ involved thermal polymerization, employing melamine as the precursor and thiourea as the source of sulfur. A total of 5 g of melamine precursor and 5 g of thiourea were combined and thoroughly ground to obtain blended mixture. The resulting product was subsequently dried at 60 °C, followed by calcination in a muffle furnace. The calcination process involved heating the mixture at a rate of 3 °C min⁻¹ until reaching a temperature of 550 °C, and maintaining this temperature for a duration of 2 h. Subsequently, S-g-C₃N₄ with a nanosheet structure was obtained. Similarly, MgAl-CLDH was prepared as follows: 3 g MgAl-LDH was placed in a muffle furnace, heated to 500 °C with a heating rate of 5 °C min⁻¹ and held for calcination for 3 h.

The S-g-C₃N₄/MgAl-CLDH photocatalytic composites were synthesized *via* electrostatic self-assembly. The preparation procedure, as depicted in Fig. 1, involved the following steps. Firstly, 0.2 g of S-g-C₃N₄ was added to a beaker containing 20 mL of anhydrous ethanol. The beaker was then subjected to ultrasonic treatment (with an ultrasonic intensity of 0.96 kW m⁻²) in a water bath for 6 h, resulting in the formation of a well-dispersed S-g-C₃N₄ suspension. Similarly, 0.5 g of MgAl-CLDH powder was dispersed in a beaker containing 50 mL of anhydrous ethanol. Subsequently, the suspensions of S-g-C₃N₄ and MgAl-CLDH were combined and placed in an oil bath at 80 °C. The mixture was stirred under sealed conditions for 12 h, followed by open stirring at 80 °C until it was completely dried, resulting in the formation of the desired S-g-C₃N₄/MgAl-CLDH photocatalytic composites.

2.3. Preparation of photocatalytic cement mortars

Both the internal mixing and coating method were adopted to prepare photocatalytic cement mortars. For the internal mixing method, S-g-C₃N₄/MgAl-CLDH (accounting for 0 wt%, 3 wt% and 5 wt% of OPC) was mixed with 135 g of deionized water. The mixture was stirred for 60 min to attain a stable suspension. In the meantime, 450 g of OPC and 1350 g of standard sand were placed into the mixer. Then, dry materials were mixed at a slow speed (140 rpm) for 1 min. Subsequently, the photocatalytic

suspension was added into the mixer within 30 s, followed by adding another 135 g of deionized water. Then, the mixture was mixed at a slow speed for 90 s and at a fast speed (285 rpm) for another 90 s. Well-mixed fresh mortar was cast into cube molds with dimensions of 40 mm × 40 mm × 40 mm. After that, the molds were put onto a vibration table for vibrating until bubbles no longer emerge on the mortar surface. During the vibration, a scraper was used to flatten the surface. At one day of curing age, mortar specimens were demolded and transferred into a standard curing room (20 ± 2 °C, >95% RH).

For the coating method, 0.5 g of Ptb emulsion was weighed and dissolved in 100 mL of deionized water and stirred rapidly for 60 min until the emulsion and water got fully mixed to obtain the binding agent. Next, 2 g of S-g-C₃N₄/MgAl-CLDH was added to the binding agent and then it was stirred for another 60 min to obtain a uniformly dispersed suspension. Cement mortar with water: cement: sand ratio of 0.6 : 1 : 3 was prepared as per Chinese standard GB/T 17671-1999. Until the age of 28 d, the mortar specimen was coated with the photocatalytic slurry. To make the surface suspension spread evenly, a fine toothpick was used to scrape the surface. The S-g-C₃N₄/MgAl-CLDH content of each layer of coating is about 0.02 g. Then, the mortar specimen was dried in an oven with a constant temperature of 60 °C for 10 min. After the coating was completely dry, the next layer of coating was applied, up to a maximum of six layers.

2.4. Characterization of physical and chemical properties

Analytical techniques including XRD, FTIR, BET, UV-vis DRS, TEM and SEM-EDX were employed to characterize the photocatalysts. To investigate the crystal plane in each photocatalyst, XRD analysis was conducted using a MiniFlex 600 (Rigaku Co., Ltd., Japan), with a voltage of 40 kV and a current of 40 mA. The diffracted intensity of K α Cu radiation was measured across a range of 2 θ from 5° to 65°, with a scanning rate of 20° min⁻¹. By FTIR spectroscopy, the functional groups and chemical bonds of dry photocatalysts were investigated using a Nicolet iS50 (Thermo Fisher Scientific China Co., Ltd.). The scanning range was 400–4000 cm⁻¹, with 64 scans and a resolution of 2 cm⁻¹. In addition, the heterojunction structure of the sample was observed by TEM using a TECNAI G2 F20 (ThermoFisher, USA). Before TEM analysis, the sample was dispersed in anhydrous ethanol and then deposited on an amorphous carbon grid. The specific surface area and pore size distribution of samples were obtained through BET test using the ASAP 2020 (Micromeritics, USA) automatic specific surface porosity analyzer. Before BET analysis, each sample was heated at 60 °C for 24 h under vacuum. The optical absorbance of dry photocatalysts was examined using a UV-vis spectrometer (Cary 7000, Agilent, USA) within the range of 200–800 nm, and BaSO₄ was used as the reference. Lastly, the morphology and element mapping of the sample was investigated by SEM-EDX, using a Verios G4 UC (ThermoFisher, USA). Prior to SEM-EDX analysis, powder samples were mounted on double-sided carbon tape and gold-plated for 2 min using a fully automatic sputter coater (Emitech K550X, USA).



2.5. Characterization of photocatalytic activity

2.5.1. Photocatalytic degradation of RhB. In a light-proof environment, 0.05 g of S-g-C₃N₄/MgAl-CLDH was added to 100 mL of RhB solution with a concentration of 10 mg L⁻¹ (C₀). The solution was stirred for 30 min using a magnetic stirrer at a constant temperature of 20 °C until the RhB and photocatalyst in the solution reached the adsorption/desorption equilibrium. At this point, the concentration of RhB was regarded as C_q. Then the beaker with the solution was put under a xenon lamp (300 W), and 5 mL of the solution was taken out every 15 min. The solid and liquid of the reaction solution was separated by a high-speed centrifuge to prevent its further degradation. Finally, the absorbance value of the sample solution at λ = 554 nm was tested, and its concentration was determined as C_t. Using eqn (1), the degradation rate δ to RhB solution was calculated.

$$\delta = \frac{C_q - C_t}{C_q} \times 100\% \quad (1)$$

2.5.2. Photocatalytic degradation of NO_x. Fig. 2 shows the customized setup for the NO_x degradation reaction. The setup mainly comprises a NO_x gas supply, a synthetic air supply, a xenon lamp (300 W), an air humidifier, a gas flowmeter, a reaction chamber and a NO_x analyzer (Gastiger 6000). NO_x and air were mixed prior to introduction into the reaction chamber (a sealed quartz glass cylindrical tube). NO_x analyzer was utilized to monitor real-time NO_x concentration of the gas out of the chamber. The NO_x degradation efficiency of the photocatalyst was assessed using the cyclic reaction method (see Fig. 2(a)), whereas the NO_x degradation efficiency of the photocatalytic mortar was evaluated using the continuous reaction method (see Fig. 2(b)).

In case of cyclic reaction method, 0.5 g of photocatalytic powder was first placed in a quartz groove (40 mm × 20 mm × 10 mm) and then a small amount of anhydrous ethanol was added for ultrasonic dispersion. Next the powder was dried and cooled to room temperature. The prepared sample was put into the reaction chamber. The mixed gas was injected into the chamber, with a gas flow rate of 0.5 L min⁻¹. In the meantime, the NO_x concentration data was recorded every 30 s. When the initial concentration of NO_x reached a stable equilibrium state, the ventilation was stopped, and the NO_x concentration value [C_{NO_x}]_{in} was recorded. To start the photocatalytic oxidation reaction, the xenon lamp was turned on. After illumination for 50 min, the xenon lamp was turn off and the NO_x concentration

value [C_{NO_x}]_{out} was recorded. Using eqn (2), the degradation rate of the photocatalyst to NO_x can be calculated.

$$\phi = \frac{[C_{NO_x}]_{in} - [C_{NO_x}]_{out}}{[C_{NO_x}]_{in}} \times 100\% \quad (2)$$

In case of continuous reaction method, the photocatalytic mortar block (40 mm × 20 mm × 5 mm) was placed into the reaction chamber. After the gas reached the preassigned concentration, dark adsorption was performed for 10 min to achieve adsorption balance. Then, the xenon lamp was turned on to activate the photocatalytic NO_x degradation reaction. The reaction time was 60 min. To regulate the light intensity of the experiment, the distance between the xenon lamp and the reaction vessel was controlled, while the NO_x gas flow rate was maintained at a constant flow rate of 0.5 L min⁻¹. Following the completion of the reaction, the xenon lamp should be deactivated until the NO_x concentration reverted to its initial instantaneous level prior to the commencement of the reaction. The experimental temperature was regulated at 25 ± 2 °C, while the humidity was maintained at 55 ± 5% RH. The degradation ratio and rate of NO_x can be calculated as follows:

$$NO_x \text{ removal ratio}(\%) = \left(\frac{NO_{x[0]} - NO_{x[i]}}{NO_{x[0]}} \right) \times 100\% \quad (3)$$

where NO_{x[0]} and NO_{x[i]} represent the initial NO_x concentration and the NO_x concentration after the photocatalytic reaction time of *i*, respectively.

$$NO_x \text{ removal rate} = \frac{f \int_0^i NO_{x[i]} - NO_{x[0]} dt}{V_i AT} \quad (4)$$

where *f* is the NO_x gas flow rate under standard conditions, *V_i* is the volume of 1 mol testing gas under standard conditions (22.4 L), *A* is the surface area of the sample, *T* is the duration of photocatalytic reaction time.

3. Results and discussion

3.1. Characterization of physicochemical properties of S-g-C₃N₄/MgAl-CLDH

3.1.1. XRD analysis. Fig. 3 illustrates the XRD patterns of g-C₃N₄, S-g-C₃N₄, MgAl-CLDH, MgAl-LDH, and S-g-C₃N₄/MgAl-CLDH.

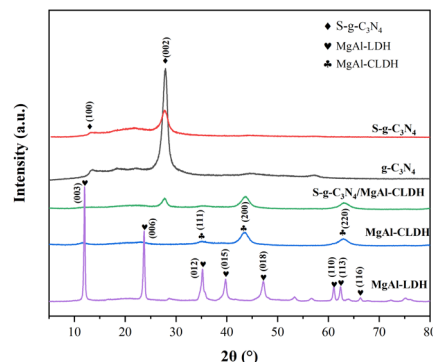


Fig. 3 XRD patterns of g-C₃N₄, S-g-C₃N₄, MgAl-CLDH, MgAl-LDH and S-g-C₃N₄/MgAl-CLDH.

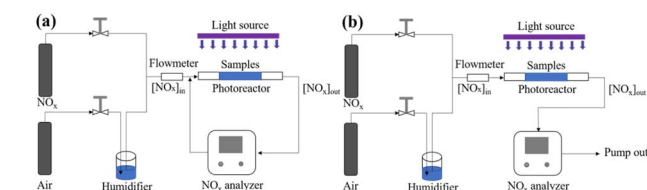


Fig. 2 Experimental setup for NO_x photocatalytic degradation test: (a) cyclic reaction; (b) continuous reaction.



CLDH nanocomposites. The characteristic diffraction peaks observed at 2θ of 13.0° and 27.3° are attributed to the crystal plane reflections of $g\text{-C}_3\text{N}_4$, which can be indexed to the (0 0 2) and (1 0 0) planes in JCPDS 87-1526.²³ Both $S\text{-g-C}_3\text{N}_4$ and $g\text{-C}_3\text{N}_4$ exhibit diffraction peaks at the same positions. However, the intensity of the diffraction peaks of $S\text{-g-C}_3\text{N}_4$ is weakened compared to that of $g\text{-C}_3\text{N}_4$, indicating a reduction in the crystallinity of $g\text{-C}_3\text{N}_4$ after sulfur doping. A similar result has been reported in a previous study.²⁴ For MgAl-LDH nanosheets, the diffraction peaks observed at 2θ of 11.71° , 23.57° , 35.02° , 39.67° , 47.09° , 60.94° and 62.35° represent the crystal plane reflections of the interlayer region containing CO_3^{2-} hydroxalite phase, corresponding to the (0 0 3), (0 0 6), (0 1 2), (0 1 5), (0 1 8), (1 1 0) and (1 1 3) planes in JCPDS 035-0964.²⁵ Subsequent to the calcination process, the diffraction patterns of MgAl-CLDH reveal peaks at 2θ of 36.94° , 42.92° and 62.3° , associated with (1 1 1), (2 0 0) and (2 2 0) planes in JCPDS 87-0653.²⁶ These peaks indicate the reflection of crystal planes within the interlayer region, suggesting the absence of the ionic hydroxalite phase. Furthermore, compared to pure MgAl-LDH , the disappearance of the major characteristic peaks of MgAl-LDH after calcination was observed, resulting in the emergence of distinct characteristic peaks of metal oxides. It is noticeable that $S\text{-g-C}_3\text{N}_4/\text{MgAl-CLDH}$ exhibits characteristic diffraction peaks corresponding to both $S\text{-g-C}_3\text{N}_4$ and MgAl-CLDH , indicating the presence of both phases in the $S\text{-g-C}_3\text{N}_4/\text{MgAl-CLDH}$ composite. No additional impurity peaks are observed in the XRD spectra, suggesting the absence of crystalline impurities in the $S\text{-g-C}_3\text{N}_4/\text{MgAl-CLDH}$, thus confirming its successful synthesis and high purity.

3.1.2. FTIR spectra. Fig. 4 depicts the FTIR spectra of $g\text{-C}_3\text{N}_4$, $S\text{-g-C}_3\text{N}_4$, MgAl-CLDH and $S\text{-g-C}_3\text{N}_4/\text{MgAl-CLDH}$ nanocomposites. It can be observed that the peak around 807 cm^{-1} in $g\text{-C}_3\text{N}_4$ corresponds to the characteristic breathing-vibration mode of the intralayer heterocyclic triazine units, forming a hexagonal structure, and the peaks between 1200 cm^{-1} to 1650 cm^{-1} correspond to the typical stretching vibrations of $\text{C}=\text{N}$ and the heterocyclic vibrations of $\text{C}-\text{N}$.²⁷ Furthermore, the spectra of $g\text{-C}_3\text{N}_4$ and $S\text{-g-C}_3\text{N}_4$ exhibit a similar profile, indicating that the sulfur doping does not alter the chemical structure of $g\text{-C}_3\text{N}_4$. The peaks observed at 509 cm^{-1} and

668 cm^{-1} in MgAl-CLDH can be attributed to the stretching vibrations of $\text{Al}-\text{O}$, while the peak at 856 cm^{-1} can be attributed to the stretching vibrations of $\text{Mg}-\text{O}$.²⁸ The characteristic peaks of $S\text{-g-C}_3\text{N}_4/\text{MgAl-CLDH}$ are similar to those of $S\text{-g-C}_3\text{N}_4$. This indicates that MgAl-CLDH is successfully loaded onto the surface of $S\text{-g-C}_3\text{N}_4$, and the chemical structure of $S\text{-g-C}_3\text{N}_4$ is not disrupted during the composite formation with MgAl-CLDH . However, the relative peak intensities in the range of 1240 cm^{-1} to 1640 cm^{-1} are much weaker in $S\text{-g-C}_3\text{N}_4/\text{MgAl-CLDH}$ than in $S\text{-g-C}_3\text{N}_4$. This could be attributed to the formation of chemical bonding between the Mg in MgAl-CLDH and the N in $S\text{-g-C}_3\text{N}_4$.²⁹ Furthermore, the FTIR spectra of the $S\text{-g-C}_3\text{N}_4/\text{MgAl-CLDH}$ sample exhibit vibrational bands corresponding to both $S\text{-g-C}_3\text{N}_4$ and MgAl-CLDH , proving the formation of a heterostructure in $S\text{-g-C}_3\text{N}_4/\text{MgAl-CLDH}$.

3.1.3. TEM analysis. To investigate the morphology and structural characteristics of the $S\text{-g-C}_3\text{N}_4/\text{MgAl-CLD}$, TEM analysis was employed, and the results are shown in Fig. 5. The MgAl-CLDH exhibits a hexagonal morphology with a lateral dimension of approximately 50 nm .³⁰ It can be observed that MgAl-LDH undergoes collapse of its structure after calcination, resulting in the formation of irregularly shaped two-dimensional nanosheets of MgAl-CLDH . The surface of $S\text{-g-C}_3\text{N}_4$ appears relatively smooth, exhibiting a typical amorphous two-dimensional nanosheet structure. By loading MgAl-CLDH onto the $S\text{-g-C}_3\text{N}_4$, the $S\text{-g-C}_3\text{N}_4/\text{MgAl-CLDH}$ heterostructure is obtained (see Fig. 5(b)). As shown in Fig. 5(c), lattice fringes with a lattice spacing of 0.21 nm are observed on the (2 2 0) crystal plane of the Mg(Al)O cubic phase,³¹ while the amorphous domains, due to their low crystallinity, are attributed to $S\text{-g-C}_3\text{N}_4$, confirming the presence of both $S\text{-g-C}_3\text{N}_4$ and MgAl-CLDH . According to what have been observed in TEM images, it is safe to say that the MgAl-CLDH nanosheets are successfully loaded onto the surface of $S\text{-g-C}_3\text{N}_4$ through electrostatic self-assembly, resulting in the formation of a heterostructure, $S\text{-g-C}_3\text{N}_4/\text{MgAl-CLDH}$. This 2D/2D heterostructure with an intact interface facilitates the transfer and separation of photo-generated charge carriers.³²

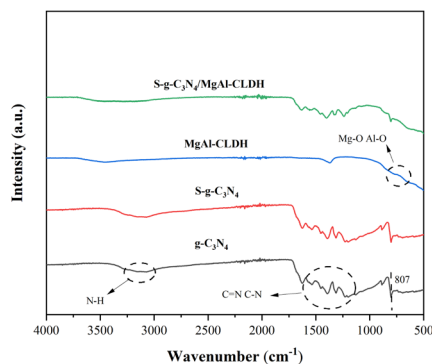


Fig. 4 FTIR spectra of $g\text{-C}_3\text{N}_4$, $S\text{-g-C}_3\text{N}_4$, MgAl-CLDH and $S\text{-g-C}_3\text{N}_4/\text{MgAl-CLDH}$.

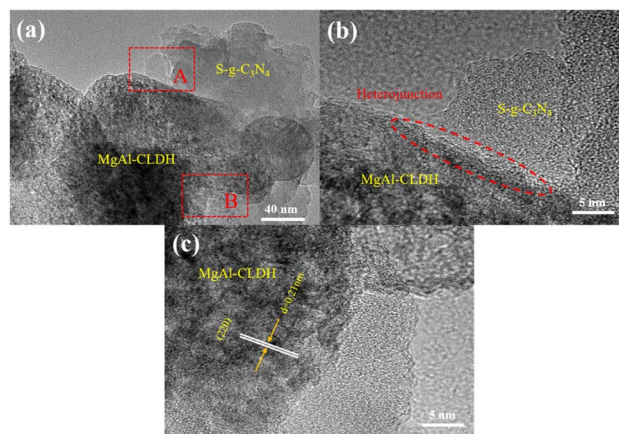


Fig. 5 TEM images of $S\text{-g-C}_3\text{N}_4/\text{MgAl-CLDH}$: (a) under low magnification; (b) section A under high magnification; (c) section B under high magnification.



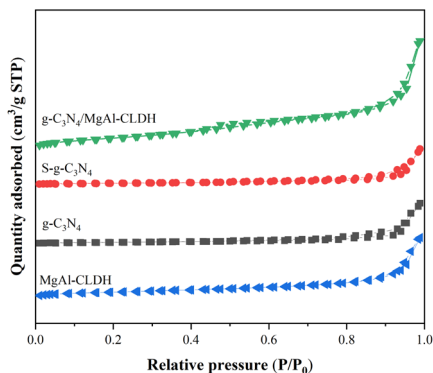


Fig. 6 Nitrogen adsorption-desorption isotherms of g-C₃N₄, S-g-C₃N₄, MgAl-CLDH and S-g-C₃N₄/MgAl-CLDH.

3.1.4. BET test. Fig. 6 presents the nitrogen adsorption-desorption isotherms of g-C₃N₄, S-g-C₃N₄, MgAl-CLDH and S-g-C₃N₄/MgAl-CLDH. The slope in the BET equation is used to calculate the amount of monolayer adsorption. In combination with the area occupied by individual molecules on the adsorbent surface, the specific surface area of the sample can be calculated. Meanwhile, the pore size distribution can be calculated according to the BJH method. Table 3 provides the pore diameter, specific surface area and pore volume of each photocatalyst. The specific surface area and pore volume of the S-g-C₃N₄ are 12.55 m² g⁻¹ and 0.023 cm³ g⁻¹, respectively. After the electrostatic loading of MgAl-CLDH nanosheets onto the surface of S-g-C₃N₄, the specific surface area and pore volume of S-g-C₃N₄/MgAl-CLDH are significantly increased, reaching respectively 2.94 times and 3.95 times that of S-g-C₃N₄. The incorporation of S-g-C₃N₄ leads to the formation of an outward-expanding structure on the surface of MgAl-CLDH, resulting in the enhanced generation of pores and an increased specific surface area of the sample. It has been reported that larger pore volume and higher specific surface area are beneficial for enhancing the absorption of UV-vis light and increasing the number of active catalytic sites.³³ The pore size distributions are derived from desorption branches of isotherms using BJH method, as shown in Fig. 7. The pore size distribution of S-g-C₃N₄ is mainly concentrated between 2 nm and 30 nm. In comparison to S-g-C₃N₄, the relative volume of large pores (>50 nm) in S-g-C₃N₄/MgAl-CLDH has significantly increased, which can enlarge the exposed surface area and enhance light utilization. Therefore, it can be inferred that the loading of MgAl-CLDH will be beneficial for improving the photocatalytic activity of S-g-C₃N₄.

Table 3 Pore size, specific surface area and pore volume of different photocatalysts

Samples	S_{BET} (m ² g ⁻¹)	Pore volume (cm ³ g ⁻¹)	Average pore diameter (nm)
g-C ₃ N ₄	7.54	0.014	18.55
S-g-C ₃ N ₄	12.55	0.023	17.32
MgAl-CLDH	54.79	0.047	9.68
S-g-C ₃ N ₄ /MgAl-CLDH	36.86	0.091	13.63

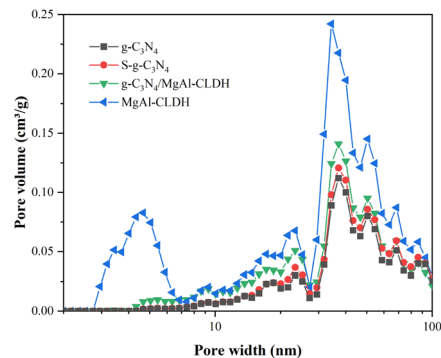


Fig. 7 Pore size distribution of g-C₃N₄, S-g-C₃N₄, MgAl-CLDH and S-g-C₃N₄/MgAl-CLDH.

3.1.5. UV-vis DRS analysis. The most critical factors governing the photocatalytic activity can be ascribed to the light absorption and the capacity for transferring excited electrons in semiconductors. The optical characteristics of the samples were determined by measuring their UV-vis DRS. Additionally, the bandgap width of the photocatalytic material was calculated using the Tauc plot function, as shown in eqn (5).³⁴

$$\alpha h\nu = K(h\nu - E_g)^{2/n} \quad (5)$$

where α represents the absorption coefficient, h represents the Planck constant, ν represents the frequency of light, K represents a proportionality constant, E_g represents the bandgap width of the photocatalytic material. Additionally, the characteristics of semiconductor electron transitions determine the exponent n (g-C₃N₄ is a direct bandgap semiconductor, allowing direct electron transitions, hence n is 1).

Fig. 8(a) and (b) show the UV-vis diffuse reflectance spectra and bandgap width curve of each photocatalyst, respectively. It can be seen that compared to g-C₃N₄, S-g-C₃N₄ exhibits a redshift in the absorption edge. Specifically, the maximum absorption edge positions of g-C₃N₄ and S-g-C₃N₄ are 455 nm and 470 nm, respectively. In addition, the widened absorption range and the heightened absorption peak observed in S-g-C₃N₄ suggest an increased capacity for light absorption. The bandgap widths of S-g-C₃N₄ and g-C₃N₄ are determined to be 2.43 eV and 2.53 eV, respectively. This indicates that sulfur doping can reduce the bandgap width of g-C₃N₄, thereby effectively

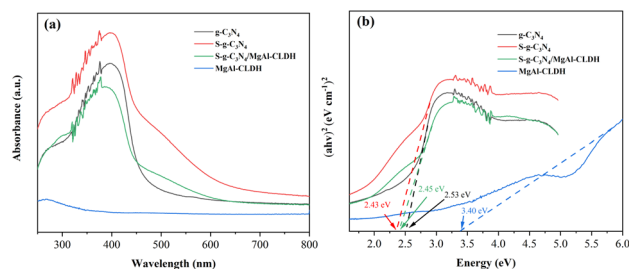


Fig. 8 (a) UV-vis absorption spectra and (b) Tauc plot of g-C₃N₄, S-g-C₃N₄, MgAl-CLDH and S-g-C₃N₄/MgAl-CLDH.



separating photogenerated electron-hole pairs and enhancing the light response range. On the other hand, the weak absorption phenomenon of the MgAl-CLDH derived metal oxide under UV light (below 400 nm) indicates its low photocatalytic performance. Compared to MgAl-CLDH and $g\text{-C}_3\text{N}_4$, the S- $g\text{-C}_3\text{N}_4$ /MgAl-CLDH shows significantly different absorption curves. Firstly, S- $g\text{-C}_3\text{N}_4$ /MgAl-CLDH exhibits a noticeable absorption band near 465 nm within the visible light range, and its bandgap width is calculated to be around 2.45 eV. Secondly, S- $g\text{-C}_3\text{N}_4$ /MgAl-CLDH demonstrates a redshift in the absorption wavelength. As a result, under the same UV-vis light absorption intensity, S- $g\text{-C}_3\text{N}_4$ /MgAl-CLDH exhibits stronger absorption in the visible light range than $g\text{-C}_3\text{N}_4$ and MgAl-CLDH. Additionally, S- $g\text{-C}_3\text{N}_4$ /MgAl-CLDH exhibits a wider absorption peak in the range of 450 nm to 550 nm. Accordingly, the electrostatic self-assembly of S- $g\text{-C}_3\text{N}_4$ with MgAl-CLDH effectively improves the material's optical properties and enhances the range of visible light absorption, and meanwhile increases light utilization efficiency and generates more photogenerated electron-hole pairs, thereby significantly enhancing the photocatalytic activity.

3.1.6. SEM-EDX analysis. Fig. 9 shows the SEM images of S- $g\text{-C}_3\text{N}_4$, MgAl-CLDH and S- $g\text{-C}_3\text{N}_4$ /MgAl-CLDH. As shown in Fig. 9(a), S- $g\text{-C}_3\text{N}_4$ exhibits an irregular two-dimensional layered structure with relatively thick layers. Additionally, the surface of S- $g\text{-C}_3\text{N}_4$ appears rough and porous, primarily due to the generation of a significant amount of carbon dioxide and ammonia during the preparation process, which promotes the formation of porous structures. Meanwhile, the MgAl-CLDH monomer consists of hexagonal shapes with relatively uniform sizes, approximately in several micrometers (see Fig. 9(b)). After the electrostatic self-assembly of S- $g\text{-C}_3\text{N}_4$ and MgAl-CLDH, it can be observed that the surface of S- $g\text{-C}_3\text{N}_4$ is loaded with a large number of MgAl-CLDH layered structures (see Fig. 9(c)). Compared to the monomer structure of S- $g\text{-C}_3\text{N}_4$, S- $g\text{-C}_3\text{N}_4$ /MgAl-CLDH nanocomposite exhibits a significantly larger particle size, enhanced porosity and irregular

morphology, promoting a face-to-face contact between the 2D materials. This facilitates an improved charge transfer rate of the photocatalyst³⁵ and provides more active sites and larger specific surface area for photocatalytic reactions.

3.2. Characterization of photocatalytic activity of S- $g\text{-C}_3\text{N}_4$ /MgAl-CLDH

3.2.1. Degradation effect of S- $g\text{-C}_3\text{N}_4$ /MgAl-CLDH on RhB.

To characterize the photocatalytic activity of different photocatalytic materials, RhB was selected as one of the pollutants, and its degradation effect is shown in Fig. 10. As can be seen, under the dark environment, the concentrations of RhB in different solution were all reduced, mainly owing to the physical adsorption on the surface of the photocatalytic materials. The $g\text{-C}_3\text{N}_4$ exhibited the lowest RhB degradation rate due to its limited light energy absorption capacity. To be specific, after 30 min of irradiation, the RhB degradation rate of $g\text{-C}_3\text{N}_4$ reached 83.1% only. However, the RhB degradation rate of S- $g\text{-C}_3\text{N}_4$ attained 88%, indicating modification with sulfur has positively contributed to the photocatalytic activity of $g\text{-C}_3\text{N}_4$. Similar results have been reported by Hu *et al.*³⁶ It is noteworthy that the S- $g\text{-C}_3\text{N}_4$ /MgAl-CLDH nanocomposite exhibits remarkable degradation ability towards RhB, particularly at an early stage. The degradation rate of S- $g\text{-C}_3\text{N}_4$ /MgAl-CLDH at 15 min was 15.67 times that of MgAl-CLDH and 1.25 times that of S- $g\text{-C}_3\text{N}_4$. Complete degradation of RhB in the solution is achieved within 30 min. The exceptional performance can be attributed to the interfacial effect between S- $g\text{-C}_3\text{N}_4$ and MgAl-CLDH, which facilitates electron separation and transfer, thus significantly enhancing the photocatalytic activity. Even after 60 min of irradiation, there still remains some residual RhB in the solution regardless of S- $g\text{-C}_3\text{N}_4$ or MgAl-CLDH as the photocatalyst.

3.2.2. Degradation effect of S- $g\text{-C}_3\text{N}_4$ /MgAl-CLDH on NO_x .

The photocatalytic activities of each photocatalyst were also investigated in terms of NO_x degradation, and the result is shown in Fig. 11. Among the tested photocatalysts, MgAl-CLDH exhibits the least photocatalytic activity, akin to the findings observed for RhB degradation. Due to the high photogenerated electron-hole pair recombination rate of $g\text{-C}_3\text{N}_4$ and its low absorption of visible light, the $g\text{-C}_3\text{N}_4$ shows the second lowest

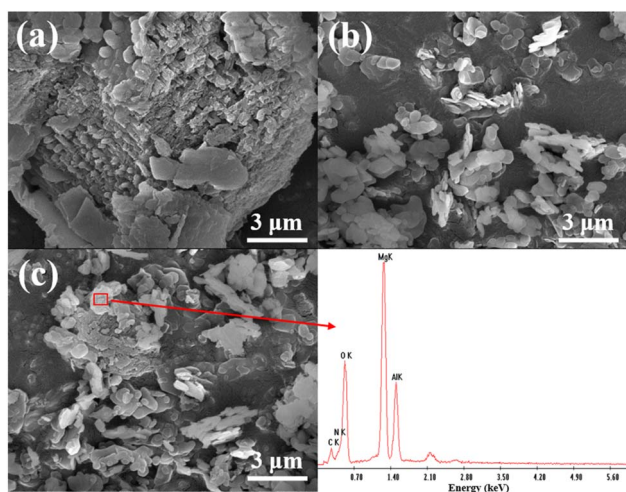


Fig. 9 SEM image: (a) S- $g\text{-C}_3\text{N}_4$; (b) MgAl-CLDH; (c) S- $g\text{-C}_3\text{N}_4$ /MgAl-CLDH.

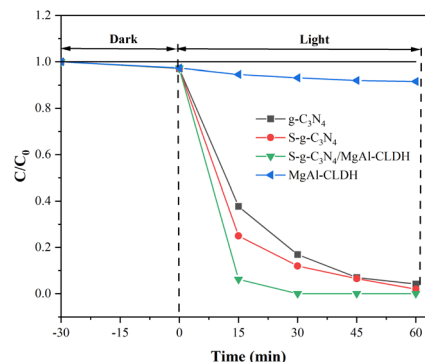


Fig. 10 Photocatalytic degradation of RhB by $g\text{-C}_3\text{N}_4$, S- $g\text{-C}_3\text{N}_4$, MgAl-CLDH and S- $g\text{-C}_3\text{N}_4$ /MgAl-CLDH.



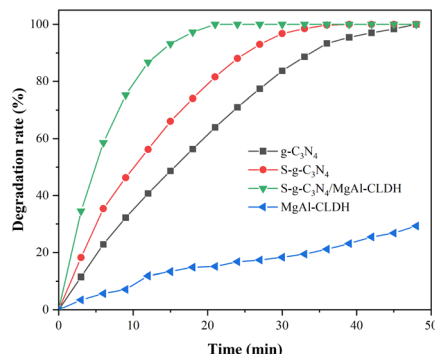


Fig. 11 Photocatalytic degradation of NO_x by $\text{g-C}_3\text{N}_4$, $\text{S-g-C}_3\text{N}_4$, MgAl-CLDH and $\text{S-g-C}_3\text{N}_4/\text{MgAl-CLDH}$.

photocatalytic performance. Conversely, the combining of sulfur brings about a specific positive influence on the photocatalytic activity of $\text{g-C}_3\text{N}_4$. After 21 min of exposure, the photocatalytic degradation rates of $\text{g-C}_3\text{N}_4$ and $\text{S-g-C}_3\text{N}_4$ reached 64.0% and 81.5%, respectively. By combining $\text{S-g-C}_3\text{N}_4$ and MgAl-CLDH , the photocatalyst ($\text{S-g-C}_3\text{N}_4/\text{MgAl-CLDH}$) with exceptional NO_x degradation ability is obtained. Specifically, the NO_x degradation rate could reach 100% at 21 min for $\text{S-g-C}_3\text{N}_4/\text{MgAl-CLDH}$. The enhanced photocatalytic performance of $\text{S-g-C}_3\text{N}_4/\text{MgAl-CLDH}$ is achieved through the reduction of the photogenerated electron-hole pair recombination rate. This reduction accelerates the photocatalytic redox reaction, resulting in an overall improvement in the photocatalytic performance.

To examine the electronic potentials of $\text{S-g-C}_3\text{N}_4$ and MgAl-CLDH , Mott-Schottky (M-S) tests were performed. The positive slope in the M-S plots indicates that both $\text{S-g-C}_3\text{N}_4$ and MgAl-CLDH have n-type semiconductor properties. According to the intersection point of slope and abscissa of the M-S plots, the flat band potentials (vs. SCE) for $\text{S-g-C}_3\text{N}_4$ and MgAl-CLDH are determined as -1.18 and -0.45 eV, respectively, which are similar to their conduction band (CB) potentials. By employing the formula $E_g = E_{\text{VB}} - E_{\text{CB}}$, the valence band (VB) values (vs. SCE) for $\text{S-g-C}_3\text{N}_4$ and MgAl-CLDH were calculated as 1.25 and 2.95 eV, respectively. Then, a possible mechanism of photocatalytic NO_x degradation by the $\text{S-g-C}_3\text{N}_4/\text{MgAl-CLDH}$ is proposed and illustrated in Fig. 12. Under light irradiation, electrons (e^-) on the surface of $\text{S-g-C}_3\text{N}_4$ in the nanocomposite

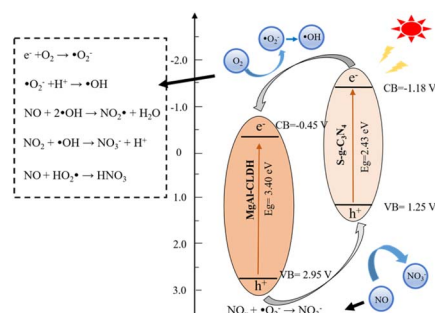


Fig. 12 Photocatalytic NO_x degradation mechanism of $\text{S-g-C}_3\text{N}_4/\text{MgAl-CLDH}$.

are excited and transiting from VB to CB. Furthermore, due to the higher CB position of $\text{S-g-C}_3\text{N}_4$ (-1.18 eV) compared to MgAl-CLDH (-0.45 eV), MgAl-CLDH acts as an efficient electron acceptor, capable of capturing electrons from the conduction band of $\text{S-g-C}_3\text{N}_4$. The photoexcited electrons are then transferred to the CB of MgAl-CLDH , accelerating electron separation and transfer, thereby enhancing the photocatalytic activity. On the surface of MgAl-CLDH , the generated electrons undergo a reduction reaction with absorbed O_2 , producing superoxide radicals (O_2^-). These radicals are then converted into hydroxyl radical (OH), which participates in catalytic oxidation reactions to degrade the target pollutant NO_x . In addition, a portion of O_2^- can directly react with the NO_x , thereby enhancing the reaction rate and promoting the separation of electrons and electron-holes (h^+).

3.2.3. Stability of $\text{S-g-C}_3\text{N}_4/\text{MgAl-CLDH}$. It has been found that elevated pH levels induce modifications in the structural characteristics of nanomaterials and surface properties, as well as the extent of ionization/dissociation pertaining to the molecules of adsorbed substances.^{37,38} The strong alkaline pore solution of cementitious materials may potentially affect the photocatalytic activity of photocatalyst. Herein, simulated concrete pore solution (SCPS) is used to evaluate the photocatalytic stability of $\text{S-g-C}_3\text{N}_4/\text{MgAl-CLDH}$.

To this end, $\text{S-g-C}_3\text{N}_4/\text{MgAl-CLDH}$ and $\text{S-g-C}_3\text{N}_4$ were immersed in two SCPS for a duration of 10 min. Subsequently, they were subjected to three cycles of rinsing with deionized water and vacuum-drying in an oven. The treated sample are denoted as $\text{S-g-C}_3\text{N}_4/\text{MgAl-CLDH}_{(\text{treated})}$ and $\text{S-g-C}_3\text{N}_4_{(\text{treated})}$. The degradation on NO_x of treated sample is shown in Fig. 13. After treatment, the degradation rate of $\text{S-g-C}_3\text{N}_4$ decreases significantly. At 12 min, the degradation rate of $\text{S-g-C}_3\text{N}_4$ is about 56.2%, and that of $\text{S-g-C}_3\text{N}_4_{(\text{treated})}$ is 40.7%, which decreases by 15.5%. In contrast, the degradation rate of $\text{S-g-C}_3\text{N}_4/\text{MgAl-CLDH}$ is 86.7%, while that of the $\text{S-g-C}_3\text{N}_4/\text{MgAl-CLDH}_{(\text{treated})}$ after SCPS treatment is 81.5%, suggesting a gentle decrease by 5.2% only. The poor chemical stability of $\text{S-g-C}_3\text{N}_4$ in SCPS may be due to the adsorption of alkaline metal ions (K^+ , Na^+ , Ca^{2+}) on the surface of the photocatalytic material in a strongly alkaline environment, leading to an increase in the rate of recombination of photogenerated electron-hole pairs

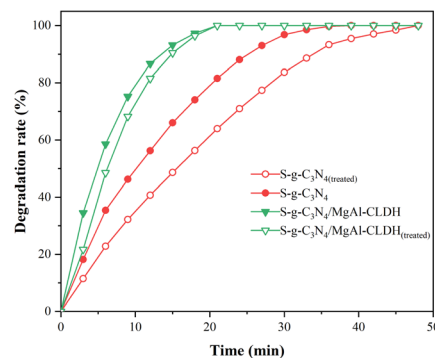


Fig. 13 Photocatalytic degradation of NO_x by $\text{S-g-C}_3\text{N}_4$ and $\text{S-g-C}_3\text{N}_4/\text{MgAl-CLDH}$ with or without SCPS treatment.

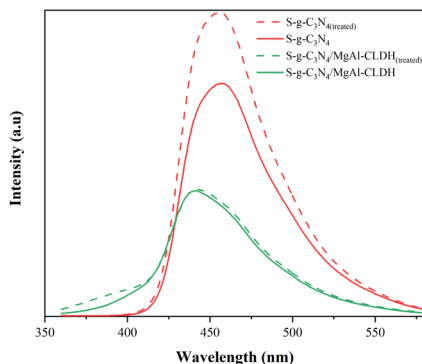


Fig. 14 PL spectra of S-g-C₃N₄ and S-g-C₃N₄/MgAl-CLDH with or without SCPS treatment.

and thus reducing the activity of the photocatalytic material.³⁹ The direct contact between S-g-C₃N₄ and the alkaline solution was avoided by combining MgAl-CLDH. As a result, the metal cations were no longer available as compounding centers for the photogenerated electron-hole pairs, effectively mitigating significant loss in photocatalytic activity.

Photoluminescence (PL) spectra serve as an effective measure to characterize the photogenerated electron-hole pair recombination rate of the photocatalyst. Fig. 14 shows the PL spectra of S-g-C₃N₄ and S-g-C₃N₄/MgAl-CLDH with or without immersion in the SCPS. It is noticeable that S-g-C₃N₄/MgAl-CLDH has much lower PL intensity compared with S-g-C₃N₄, indicating lower photogenerated electron-hole pair recombination rate. In addition, the PL intensity of S-g-C₃N₄ is significantly enhanced after treatment, indicating that the S-g-C₃N₄ is susceptible to the strong alkaline environment. The photogenerated electron-hole pair recombination rate of S-g-C₃-N₄(treated) is increased and its photocatalytic activity is adversely affected. Similar result has been reported elsewhere.⁴⁰ In contrast, the PL intensity of the S-g-C₃N₄/MgAl-CLDH material was only slightly enhanced after treatment, suggesting that S-g-C₃N₄/MgAl-CLDH has a high stability in SCPS. This can be attributed to the similarity of the structure of LDH with the hexagonal-layered hydration products of cement, including C₂(A,F)H₈, C₄(A,F)H₁₃ and C₄(A,F)H₁₉.⁴¹ Thus, MgAl-CLDH demonstrates excellent compatibility with cementitious materials and possesses favorable chemical stability in SCPS. Consequently, the introduction of MgAl-CLDH into S-g-C₃N₄ ensures that S-g-C₃N₄/MgAl-CLDH inherits respective advantages, weakening the adverse effects of highly alkaline environment on the photocatalytic activity of S-g-C₃N₄/MgAl-CLDH.

3.3. Photocatalytic activity in cement mortar

Fig. 15(a) shows the NO_x degradation curves of mortars internally mixed with S-g-C₃N₄/MgAl-CLDH. An instantaneous decrease in NO_x gas concentration at the onset of the photocatalytic reaction is observed. As the concentration of the photocatalyst increases, the decline in NO_x gas concentration becomes more pronounced. Notably, when the dosage of S-g-C₃N₄/MgAl-CLDH reaches 5 wt%, the instantaneous reduction in NO_x concentration is the highest.

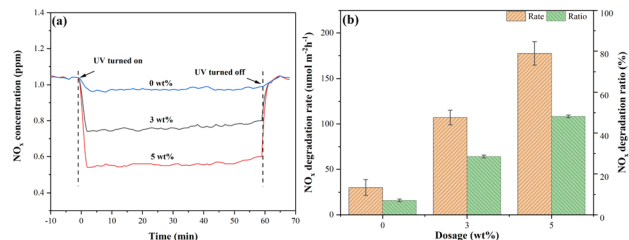


Fig. 15 (a) NO_x degradation curves and (b) NO_x degradation rate and ratio of mortar internally mixed with different S-g-C₃N₄/MgAl-CLDH concentrations.

Based on the data presented in Fig. 14(a), the NO_x degradations for cement mortar with different S-g-C₃N₄/MgAl-CLDH concentrations were calculated using eqn (3) and (4) given in Subsection 2.5.2. The results are shown in Fig. 15(b). To be specific, the NO_x degradation rates for mortars containing 0 wt%, 3 wt% and 5 wt% of S-g-C₃N₄/MgAl-CLDH are 30.1, 107.1 and 177.5 μmol m⁻² h⁻¹, respectively. Similarly, the NO_x degradation ratios for the corresponding mortars are 7.2%, 28.53% and 48.2%, respectively. This indicates that the increase in the dosage of S-g-C₃N₄/MgAl-CLDH results in an increase in the NO_x degradation rate of photocatalytic cement mortar. The observed phenomenon can be attributed to the constrained accessibility of active sites of the photocatalyst embedded in the cementitious matrix at lower concentrations of S-g-C₃N₄/MgAl-CLDH. Nevertheless, with the increase of S-g-C₃N₄/MgAl-CLDH content, the population of active sites on the surface of the cementitious material increases, thus progressively enhancing its ability to degrade NO_x through photocatalysis. Notably, photocatalytic mortar with 5 wt% S-g-C₃N₄/MgAl-CLDH exhibits the highest NO_x degradation rate and ratio.

Fig. 16(a) shows the NO_x degradation curves of mortars coated with S-g-C₃N₄/MgAl-CLDH. With the increase of coating layers, the magnitude of instantaneous NO_x concentration reduction shows an initial increase followed by a decrease. To be specific, at 5 layers of coating, the greatest reduction in NO_x concentration is achieved. Fig. 16(b) shows the NO_x degradation rate and degradation ratio of photocatalytic cement mortar under different coating layers. It is obvious that the photocatalytic cement mortar coated with 5 layers of S-g-C₃N₄/MgAl-CLDH exhibits the highest NO_x degradation rate of 244.41 μmol m⁻² h⁻¹ and a degradation ratio of 68.5%. In comparison,

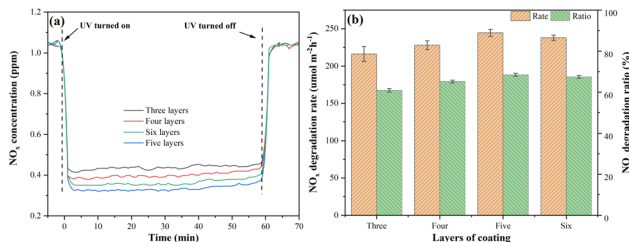


Fig. 16 (a) NO_x degradation curves and (b) NO_x degradation rate and ratio of mortar coated with S-g-C₃N₄/MgAl-CLDH under different coating layers.



the mortar with 3 layers of S-g-C₃N₄/MgAl-CLDH shows the lowest NO_x degradation rate and degradation ratio, as 216.29 μmol m⁻² h⁻¹ and 61.5%, respectively.

The reason for the aforementioned phenomenon is described as follows. When the surface of the cement mortar is coated with a small quantity of photocatalytic material, the light absorption characteristics of the S-g-C₃N₄/MgAl-CLDH coating layer are weak, leading to fewer absorbed photons and fewer generated reactive oxygen species (ROS), resulting in low photocatalytic activity. For higher coating amount of S-g-C₃N₄/MgAl-CLDH on the cementitious substrate surface, the light absorption characteristics of the coating layer is enhanced, resulting in an increased generation of ROS and an improvement in photocatalytic activity. Additionally, the thickness of the S-g-C₃N₄/MgAl-CLDH coating layer is also a crucial factor controlling the electron transfer and light absorption efficiency. When the coating reaches a certain thickness, the light absorption efficiency of the photocatalytic cementitious material saturates, and the photocatalytic activity reaches a plateau. In addition, multiple coatings on the cementitious surface gradually reduce the porosity, leading to a decline in its adsorption capacity. The degradation of NO_x in the cementitious material is a synergistic effect of its adsorption and degradation. A decrease in adsorption performance results in a reduction of internal NO_x concentration. Therefore, after 5 layers of coating, the photocatalytic capacity for NO_x degradation in the coated mortar gradually declines with further increase of coating.

The effects of the internal mixing and coating method on the degradation of NO_x in cement mortar were further elucidated by investigating the distribution of S-g-C₃N₄/MgAl-CLDH on the surface of the cement mortar. Fig. 17 shows the SEM images of mortar coated with 5 layers of S-g-C₃N₄/MgAl-CLDH and internally mixed with 5 wt% S-g-C₃N₄/MgAl-CLDH. The surface of the mortar coated with S-g-C₃N₄/MgAl-CLDH is dominated by nitrogen (N), which is rich in S-g-C₃N₄/MgAl-CLDH, while the concentration of calcium (Ca) is very low. This indicates that S-g-C₃N₄/MgAl-CLDH is evenly scattered on the surface of cement mortar and the loading amount is abundant. The increased exposure of S-g-C₃N₄/MgAl-CLDH on the surface of the cement mortar provides more opportunities for contact with NO_x, thereby facilitating the photocatalytic oxidation reaction. Whereas, the surface of mortar internally mixed with S-g-C₃N₄/MgAl-CLDH is rich in Ca and poor in N, suggesting insufficient

loading amount. It is concluded that in terms of photocatalytic performance, the coating method is more efficient, resulting in higher NO_x degradation.

4. Conclusions

A novel photocatalytic nanocomposite S-g-C₃N₄/MgAl-CLDH was prepared using electrostatic self-assembly method. The application potential of S-g-C₃N₄/MgAl-CLDH in cement-based materials was evaluated based on measurements of physico-chemical properties, photocatalytic performances and chemical stability of S-g-C₃N₄/MgAl-CLDH after immersing in simulated concrete pore solution (SCPS). Besides, photocatalytic performances of cement mortars loaded with S-g-C₃N₄/MgAl-CLDH were investigated. The main conclusions can be drawn as follows:

(1) A significant change in the lattice spacing between S-g-C₃N₄ and MgAl-CLDH was revealed by TEM technique and the formation of a heterogeneous structure between the two materials was confirmed. The successful synthesis of S-g-C₃N₄/MgAl-CLDH with high degree of crystallinity was demonstrated by XRD and FTIR.

(2) Compared to S-g-C₃N₄, the S-g-C₃N₄/MgAl-CLDH exhibited a narrower bandgap (2.45 eV), a lower rate of photo-generated electron-hole pairs recombination and a 1.94-fold increase in specific surface area. After 30 min of visible light irradiation, the degradation rate of RhB by S-g-C₃N₄ reached 88% only, whereas S-g-C₃N₄/MgAl-CLDH achieved a complete degradation of NO_x. After 21 min of visible light irradiation, the NO_x degradation rate of S-g-C₃N₄/MgAl-CLDH achieved 100% while that of S-g-C₃N₄ was merely 81.5%.

(3) After being submerged in SCPS, the photocatalytic NO_x degradation efficiency of S-g-C₃N₄ was decreased by 15.5% after 12 min of illumination, whereas S-g-C₃N₄/MgAl-CLDH exhibited only a slight decrease of 5% in degradation efficiency. The superior photocatalytic stability of S-g-C₃N₄/MgAl-CLDH is verified, which can be attributed to the excellent compatibility and stability of MgAl-CLDH in SCPS. Meanwhile, MgAl-CLDH serves as a barrier avoiding the direct contact of S-g-C₃N₄ and alkaline substances.

(4) The photocatalytic performance of the internally mixed mortar in degrading NO_x improves gradually with an increase in the dosage of S-g-C₃N₄/MgAl-CLDH. The mortar with 5 wt% of S-g-C₃N₄/MgAl-CLDH exhibits the highest NO_x degradation rate, reaching 48.2%. The NO_x degradation performance of mortar improves as the coating increases up to 5 layers, but a decline in NO_x degradation rate after 5 layers of coating is found owing to the reduced porosity of mortar because of excessive coating.

(5) In terms of photocatalytic performance, the coating method is more efficient, enabling higher NO_x degradation, than the internal mixing method.

Author contributions

Conceptualization, Z. Y., X. X. and Y. Z.; data curation, Z. Y., X. X. and S. L.; formal analysis, Z. Y. and X. X.; investigation, X. X. and S. L.; methodology, Z. Y. and X. X.; project administration,

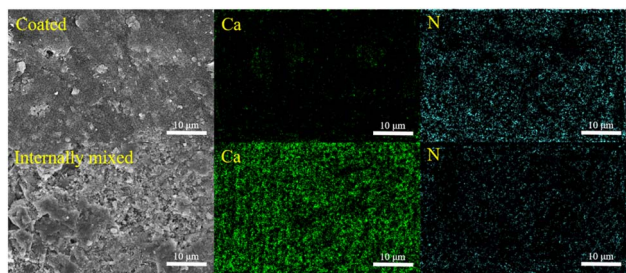


Fig. 17 SEM images and elemental mapping analyses of the mortar coated or internally mixed with S-g-C₃N₄/MgAl-CLDH.



Y. Z., B. B. and G. C. M.; supervision, Y. Z., B. B. and G. C. M.; validation, Y. Z. and S. L.; writing-original draft, Z. Y. and X. X.; writing-review and editing, Y. Z. All authors have read and agreed to the published version of the manuscript.

Conflicts of interest

The authors declare that they have no known competing financial interests or personal relationships that could have appeared to influence the work reported in this paper.

Acknowledgements

This work was financially supported by National Natural Science Foundation of China (51978171), Fujian Ocean and Fishery Bureau (FJHJF-L-2022-19) and Fuzhou Science and Technology Bureau (2021-P-031).

References

- 1 X. Lu, X. Ye, M. Zhou, Y. Zhao, H. Weng, H. Kong, K. Li, M. Gao, B. Zheng and J. Lin, *Nat. Commun.*, 2021, **12**, 5021.
- 2 B. Gu, L. Zhang, R. Van Dingenen, M. Vieno, H. J. Van Grinsven, X. Zhang, S. Zhang, Y. Chen, S. Wang and C. Ren, *Sci*, 2021, **374**, 758–762.
- 3 A. Gopalan, J. Lee, G. Saianand, K. Lee, P. Sonar, R. Dharmarajan, Y. Hou, K. Ann, V. Kannan and W. Kim, *Nanomater*, 2020, **10**, 1854.
- 4 W. Liu, S. Wang, J. Zhang and J. Fan, *Constr. Build. Mater.*, 2015, **81**, 224–232.
- 5 H. Yang, J. Zhou, Z. Duan, X. Liu, B. Deng, J. Fang and W. Xu, *Appl. Catal., B*, 2022, **310**, 121299.
- 6 S. Qi, X. Liu, R. Zhang, Y. Zhang and H. Xu, *Inorg. Chem. Commun.*, 2021, **133**, 108907.
- 7 H. Fang, X. Zhang, J. Wu, N. Li, Y. Zheng and X. Tao, *Appl. Catal., B*, 2018, **225**, 397–405.
- 8 Z. Wu, Y. Zhao, L. Mi, Y. Guo, H. Wang, K. Liu, K. Zhang and B. Wang, *Colloids Surf.*, 2021, **624**, 126756.
- 9 T. Song, X. Yu, N. Tian and H. Huang, *Int. J. Hydrogen Energy*, 2021, **46**, 1857–1878.
- 10 C. Liu, Y. Zhang, F. Dong, A. H. Reshak, L. Ye, N. Pinna, C. Zeng, T. Zhang and H. Huang, *Appl. Catal., B*, 2017, **203**, 465–474.
- 11 K. Wang, Q. Li, B. Liu, B. Cheng, W. Ho and J. Yu, *Appl. Catal., B*, 2015, **176**, 44–52.
- 12 Y. Wang, Z. Wang, S. Muhammad and J. He, *CrystEngComm*, 2012, **14**, 5065–5070.
- 13 R. Zhong, Z. Zhang, H. Yi, L. Zeng, C. Tang, L. Huang and M. Gu, *Appl. Catal., B*, 2018, **237**, 1130–1138.
- 14 J. Xiong, G. Xiao, H. Zeng, C. Chen and D. An, *Appl. Clay Sci.*, 2020, **193**, 105669.
- 15 X. Zheng, Q. Zhu, H. Peng, Y. Quan and J. Wen, *Chem. Phys. Lett.*, 2021, **779**, 138846.
- 16 M. Majdoub, Z. Anfar and A. Amedlous, *ACS Nano*, 2020, **14**, 12390–12469.
- 17 T. U. Haq and Y. Haik, *ACS Sustainable Chem. Eng.*, 2022, **10**, 6622–6632.
- 18 Z. Yang, H. Fischer and R. Polder, *Cem. Concr. Compos.*, 2014, **47**, 87–93.
- 19 Z. Yang, H. Fischer and R. Polder, *Cem. Concr. Compos.*, 2015, **58**, 105–113.
- 20 S. Sanati and Z. Rezvani, *Chem. Eng. J.*, 2019, **362**, 743–757.
- 21 H. Li, J. Li, C. Xu, P. Yang, D. H. Ng, P. Song and M. Zuo, *J. Alloys Compd.*, 2017, **698**, 852–862.
- 22 M. Huang, Z. Yang, L. Lu, J. Xu, W. Wang and C. Yang, *Catal*, 2022, **12**, 443.
- 23 L. Ge, C. Han and J. Liu, *Appl. Catal., B*, 2011, **108**, 100–107.
- 24 W. Yan, R. Zhang, F. Ji and C. Jing, *J. Hazard. Mater.*, 2020, **392**, 122472.
- 25 G. Gao, Z. Zhu, J. Zheng, Z. Liu, Q. Wang and Y. Yan, *J. Colloid Interface Sci.*, 2019, **555**, 1–10.
- 26 X. Zheng, M. Huang, Y. You, X. Fu, Y. Liu and J. Wen, *Chem. Eng. J.*, 2018, **334**, 1399–1409.
- 27 Q. Chen, S. Li, H. Xu, G. Wang, Y. Qu, P. Zhu and D. Wang, *Chin. J. Catal.*, 2020, **41**, 514–523.
- 28 D. Ivánová, P. Albert and J. Kavuličová, *Appl. Clay Sci.*, 2018, **152**, 65–72.
- 29 L. Ge, Z. Peng, W. Wang, F. Tan, X. Wang, B. Su, X. Qiao and P. K. Wong, *J. Mater. Chem. A*, 2018, **6**, 16421–16429.
- 30 Q. Song, Y. Zhou, J. Hu, C. Zhou, X. Shi, D. Li and D. Jiang, *Appl. Surf. Sci.*, 2021, **563**, 150369.
- 31 H. H. Peng, J. Chen, X. L. Guo, H. Chen and Y. X. Zhang, *Dalton Trans.*, 2016, **45**, 10530–10538.
- 32 J. Li, X. Li, G. Wu, J. Guo, X. Yin and M. Mu, *J. Environ. Chem. Eng.*, 2021, **9**, 106723.
- 33 C. Qin, Z. Li, G. Chen, Y. Zhao and T. Lin, *J. Power Sources*, 2015, **285**, 178–184.
- 34 M. Alvarez, T. López, J. A. Odriozola, M. A. Centeno, M. I. Domínguez, M. Montes, P. Quintana, D. H. Aguilar and R. D. González, *Appl. Catal., B*, 2007, **73**, 34–41.
- 35 M. Yu, L. Zhang, J. Wen, H. Zhang, F. Liu, Y. Lv and X. Zhao, *J. Inorg. Organomet. Polym.*, 2021, 1–11.
- 36 S. Hu, L. Ma, F. Li, Z. Fan, Q. Wang, J. Bai, X. Kang and G. Wu, *RSC Adv.*, 2015, **5**, 90750–90756.
- 37 T. Guan, L. Fang, Y. Lu, F. Wu, F. Ling, J. Gao, B. Hu, F. Meng and X. Jin, *Colloids Surf., A*, 2017, **529**, 907–915.
- 38 E. M. Seftel, M. Niarchos, C. Mitropoulos, M. Mertens, E. F. Vansant and P. Cool, *Catal. Today*, 2015, **252**, 120–127.
- 39 F. Peng, Y. Ni, Q. Zhou, J. Kou, C. Lu and Z. Xu, *Constr. Build. Mater.*, 2018, **179**, 315–325.
- 40 P. Liu, Y. Gao, F. Wang, W. Zhang, L. Yang, J. Yang and Y. Liu, *Constr. Build. Mater.*, 2016, **120**, 42–47.
- 41 Z. Yang, H. Fischer and R. Polder, *Mater. Corros.*, 2013, **64**, 1066–1074.

